

## Influence of Seawater on the Carbon Steel Initial Corrosion Behavior

Yuwei Liu<sup>1,2\*</sup>, Zhenyao Wang<sup>1\*</sup>, Yinghua Wei<sup>1</sup>

<sup>1</sup> Institute of Metal Research, Chinese Academy of Sciences, Wencui Rd 62, Shenyang, 110016, PR China

<sup>2</sup> School of Materials Science and Engineering, University of Science and Technology of China, Wencui Rd 62, Shenyang, 110016, PR China

\*E-mail: [ywliu12s@imr.ac.cn](mailto:ywliu12s@imr.ac.cn), [zhywang@imr.ac.cn](mailto:zhywang@imr.ac.cn)

Received: 3 August 2018 / Accepted: 12 November 2018 / Published: 5 January 2019

---

In this study, the influence of seawater on the carbon steel initial corrosion behavior, exposed to the high temperature, high humidity, and high salt marine atmosphere of the south sea, is investigated using the weight loss measurement, a stereomicroscope, a laser scanning confocal microscope (LSCM), a scanning electron microscope (SEM), X-ray diffraction (XRD), infrared spectroscopy (IRS), potentiodynamic polarization, and in-situ electrochemical impedance spectroscopy (EIS). According to the results, the kinetics of corrosion process is an accelerating process following the empirical equation  $D = At^n$ . The composition of the rust layer was mainly consisted of  $\beta$ -FeOOH,  $\gamma$ -FeOOH,  $\delta$ -FeOOH,  $\alpha$ -FeOOH, and  $Fe_3O_4$  for all corrosion periods. The existence of many voids and microcracks in rust layer and the variation of surface roughness resulted in the rust without protective effect. With the increase in the corrosion time, the charge transfer resistance decreased, whereas the corrosion current density and the corrosion rate increased gradually.

---

**Keywords:** Carbon steel; Seawater; LSCM; In-situ EIS

### 1. INTRODUCTION

Carbon steel is the most commonly used traditional structural material in construction, transportation, resource environment, and energy power infrastructures. In most cases, carbon steel is inevitably exposed to the atmosphere directly during its utility, resulting in atmospheric corrosion, which causes 50% of the total corrosion loss [1]. Owing to this reason, test methods such as natural outdoor exposure [1-5] and laboratory testing [6-8] were commonly used to evaluate the atmospheric corrosion behavior of carbon steel.

The outdoor exposure is a common test method used to investigate the comprehensive influence of the environmental factors. It can provide the most direct and reliable information about the atmospheric corrosion of metals in specific environments. However, the process is always time-consuming. Unlike, the laboratory-accelerated tests can effectively provide reliable information in a short period of time and can be used to assess the life of metallic structures under utility. Among several indoor accelerated testing methods, the wet—dry cyclic accelerated testing is proved to be a better method as it can reflect the key characteristics of atmospheric environment [9]. As atmospheric corrosion is primarily a failure process, caused by the electrochemical or chemical reaction of metallic structures with atmospheric environment during their utility, the instantaneous monitoring of atmospheric corrosion based on electrochemical measurements has received much attention, such as atmospheric corrosion monitors (ACM) [10-12] and Kelvin probes [13, 14]. However, these methods neither provide direct information about electrochemical processes nor become adaptable to the outdoor monitoring. The in-situ electrochemical impedance spectroscopy (EIS) technique has a great advantage as a non-destructive procedure and can successfully provide direct and instantaneous information on the corrosion behavior of metals [9, 15, 16].

The south sea, a kind of marine atmosphere, has the worst marine environmental conditions, showing a typical high temperature, high humidity, and high salinity environment (the so-called “three highs” environment). The synergy of these factors directly influences the process of atmospheric corrosion of metals, particularly the initial corrosion behavior.

Currently, there is a lack of research work on the initial corrosion behavior of carbon steel exposed to “three highs” environment. Surnam et al [4] stated that atmospheric corrosion in a high relative humid environment depends mainly on the time of exposure and the carbon content of carbon steel. Lan et al [5] discussed about the carbon steel being exposed to a tropical environment with high temperature, high humidity, and high frequency of rain. Further, the basic information concerning the carbon steel resistance to atmospheric corrosion in “three highs” atmosphere is not readily available. Compared to the simulated solutions, using seawater as the corrosive medium is the most realistic option as it can directly reveal the interaction between ions in seawater. A laser scanning confocal microscope (LSCM) can effectively provide information about the three-direction morphology and surface roughness of the rust layer through a non-contact method, which again has not been preferred by scholars. In addition, carbon steel often have different layers [2, 17, 18], and it is of great importance to acquire the relation between the evolution and properties of corrosion products, which are vital for predicting the long-term corrosion behavior of steel structures.

Consequently, in this study, the initial corrosion behavior of carbon steel in “three highs” atmosphere of the south sea, where temperature, relative humidity, and salinity are controlled by wet—dry cycles and seawater is investigated using the weight loss measurement, a stereomicroscope, a LSCM, a scanning electron microscope (SEM), X-ray diffraction (XRD), infrared spectroscopy (IRS), potentiodynamic polarization, and in-situ EIS.

## 2. EXPERIMENTAL

### 2.1 Material preparation

The test samples of carbon steel (Q235) contain (in mass %) 0.22 C, 0.08 Si, 0.10 Mn, 0.015 P, 0.003 S, and Fe. The size of samples for weight loss measurement was 50 mm × 25 mm × 5 mm. Prior to use, these samples were cleaned in acetone and alcohol, then dried, weighed, and stored in a desiccator. The size of samples for electrochemical experiment was 10 mm × 10 mm × 5 mm. The electrochemical test samples were wet-polished with 2000# grade SiC paper, cleaned in acetone and distilled water, and then dried.

### 2.2 Characterization of corrosion products

The morphology of the rust layers was conducted using a stereomicroscope (Zeiss Stemi 508) and scanning electron microscope (Philips XL30FEG). The 3D surface roughness was measured using a non-contact LSCM (Zeiss LSM-700), and the rust composition was analyzed using the IRS and XRD. To perform the IRS analysis, the range of spectra was taken as 400 cm<sup>-1</sup>–4000 cm<sup>-1</sup>, and the XRD measurements were obtained using Cu K $\alpha$  target at 50 kV and 250 mA with a range of 10°–90° and a scanning speed of 2° min<sup>-1</sup>.

### 2.3 Wet-dry cyclic accelerated test

The accelerated corrosion process was tested using C4-180 test system to realize the wet—dry cycle. This cycle testing involved two steps within a period of 24 h: (1) uniformly depositing 20  $\mu$ L/cm<sup>2</sup> seawater (the major components are listed in Table 1) on the surface of the samples and then drying the samples in oven at 45° C, (2) putting the samples in the test system and running the program (30° C, 90% RH for 1 h and 30° C, 60% RH for 2 h) eight times. The steps (1) and (2) were repeated for several days. Samples were analyzed after corrosion for 48 h, 96 h, 144 h, 192 h, and 288 h. For gravimetric experiments, the rusted samples were immersed in a solution containing 500 mL (38 wt.%) hydrochloric acid, 500 mL distilled water, and 3.5 g hexamethylenetetramine at ambient temperature until the corrosion products were completely removed.

**Table 1.** The main element composition of the seawater (g/L, pH 6.6)

element	Cl <sup>-</sup>	SO <sub>4</sub> <sup>2-</sup>	K <sup>+</sup>	Na <sup>+</sup>	Ca <sup>2+</sup>	Mg <sup>2+</sup>
content	20	2.18	5	10	0.3	1

### 2.4 Electrochemical measurements

The polarization curves were obtained using PARSTAT 2273 with a classical three-electrode system: platinum as the auxiliary electrode, saturated calomel electrode as the reference electrode, and rusted samples as the working electrode. Na<sub>2</sub>SO<sub>4</sub> solution of molar concentration 0.1 mol/L was chosen as the electrolyte. The sweep rate was 0.3333 mV/s.

The EIS measurements were tested using a two-electrode (electrode material was Q235) system with the surface area of approximately 2.25 cm<sup>2</sup>, as shown in Figure 1. During the test process, one electrode worked as the working electrode, and the other as the reference electrode and auxiliary electrode. The amplitude of AC voltage was 10 mV and the frequency range was 10<sup>5</sup> Hz ~ 10<sup>-2</sup> Hz.

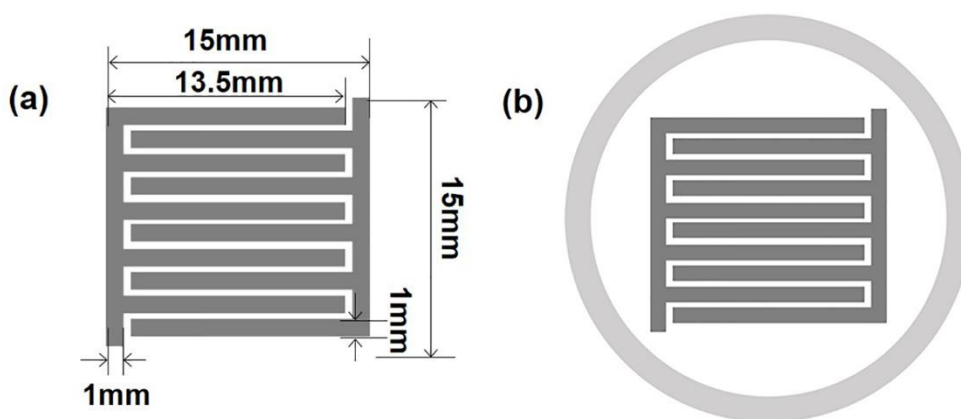


**Figure 1.** Schematic diagram in illustrating the arrangement of the micro-electrodes used for EIS measurement: (a) Top view of comb-like electrodes. (b) Top view and transverse cross-section view of the embedded electrodes.

## 3. RESULTS AND DISCUSSION

### 3.1 Thickness loss and corrosion rate

The initial corrosion kinetics of carbon steel can be identified by measuring the mass loss during the corrosion process. The thickness loss data is usually used to evaluate the corrosion rate due to the uniform corrosion of carbon steel. The thickness loss of the carbon steel samples can be calculated using the following equation[19]:

$$D = \frac{10000W_t}{\rho S} \tag{1}$$

where  $D$  is the thickness loss ( $\mu\text{m}$ ),  $W_t$  is the weight loss (g),  $\rho$  is the density ( $7.86 \text{ g/cm}^3$ ) of the carbon steel, and  $S$  is the exposed area ( $\text{cm}^2$ ) of the sample. Apparently, the thickness loss increases gradually with the increase in corrosion time. The relationship between thickness loss data and corrosion time can be fitted by using a power function [5, 20], as shown in Figure 2 (a).

$$D = At^n \tag{2}$$

where  $D$  is the thickness loss ( $\mu\text{m}$ ),  $t$  is the corrosion time (hour), and  $A$  and  $n$  are constants. The closer the  $R^2$  value is to 1, the better is the fitting result of Equation (2). As known, the  $n$  value of the fitting function reflects the protective value of the rust layer. If  $n > 1$ , the rust layer is not protective and the corrosion rate increases gradually. If  $n < 1$ , the rust layer is protective and the corrosion rate decreases and if  $n = 1$ , the corrosion rate is a constant. In this study, the value of  $n$  was 1.142, showing that the corrosion process of carbon steel was an accelerated process[21] .

To further analyze the corrosion rate, the instantaneous corrosion rate ( $V_d$ ) was obtained using the following equation [22, 23] based on Equation (2)

$$V_d = \frac{d\Delta D}{dt} = Ant^{n-1} \tag{3}$$

where  $V_d$  is the instantaneous corrosion rate ( $\mu\text{m}/\text{hour}$ ), and  $t$ ,  $D$ ,  $A$  and  $n$  are the same as mentioned above. Figure 2 (b) shows the variation of  $V_d$  with the corrosion time. It can be seen that the corrosion rate initially increased gradually, which indicates that the corrosion products have no protective effect. This destruction process may be caused due to the composition and/or structure of the corrosion products, which is discussed in next section.

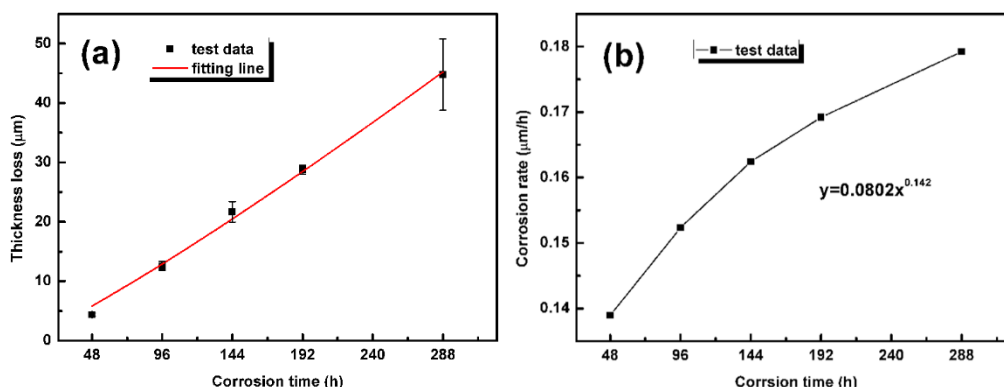


**Figure 2.** (a) Thickness loss of carbon steel samples as a function of corrosion time and (b) instantaneous corrosion rate ( $V_d$ ) of carbon steel samples as a function of corrosion time.

### 3.2 Morphology of rust layers

The macroscopic morphologies of carbon steel samples after 48 h and 288 h were observed using a stereomicroscope and a LSCM. These morphologies can provide the most intuitive information of the rust layer. It can be seen from figures 3(a) and 3(b) that the rust layers have different colors, which mean different forms. This occurred due to the accumulation of corrosion products on the surface of the substrate during a prolonged exposure time. The LSCM can provide the roughness information of the rust layer surface. All the results were obtained for the same parameter and the same size of area (approximately 9 mm  $\times$  9 mm). Figure 3(a') and 3(b') show the roughness characteristics of three-dimensional pictures and two-dimensional curves at different corrosion times. The scales of the roughness at both 48 h and 288 h show heterogeneous and wide range properties. Compared to the roughness at 48 h, the roughness curves at 288 h reflect fewer fluctuations, indicating the generation of

characteristics of many large voids. Moreover, the peaks at 48 h are steeper than those at 288 h, indicating that the corrosion process has become uniform.

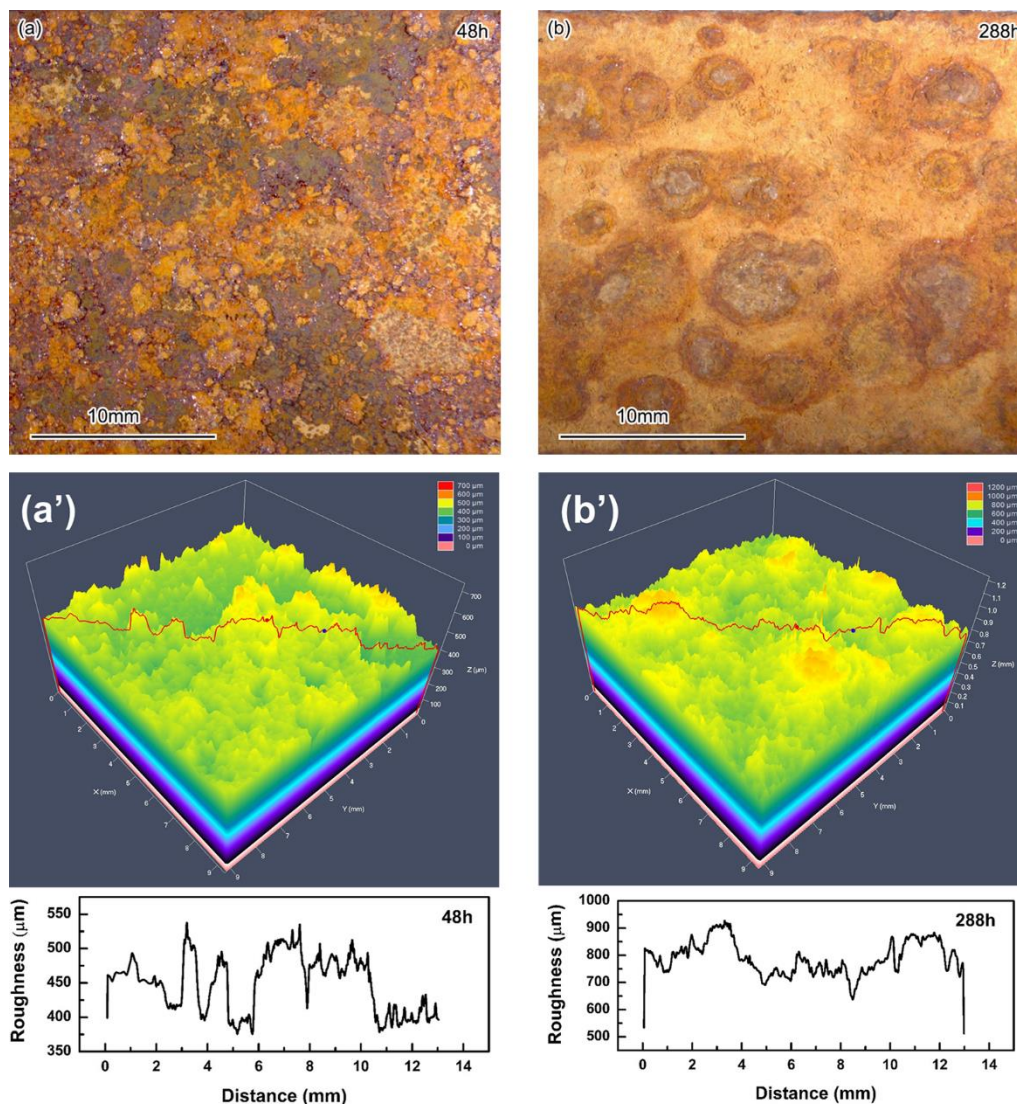


**Figure 3.** Macroscopic morphology after (a) 48 h and (b) 240 h, and 3D surface roughness after (a') 48 h and (b') 240 h.

To obtain further detailed characteristics, a SEM was used to represent the micro morphologies of the corrosion products. Figure 4. shows that the rust layers were comprised of many voids and microcracks. These voids promoted the accumulation of the seawater, replenishing the corrosive medium in the process of the corrosion, whereas the microcracks facilitated the penetration of the corrosive solution into the substrate and also accelerated the corrosion process. The energy dispersive spectroscopy (EDS) analysis results provided the elemental contents of the marked sites, A to E, as summarized in Table 2. It can be seen from Table 2. that the content of chlorine was much higher in sites C and D than in sites A, B, and E, which might be due to the residual deposits of salt in the rust layer. Small amounts of sulphur (S) and magnesium (Mg) were detected after 288 h. The results showed that chlorine was present in an abundant amount in the whole process of corrosion, and hence in the presence of a high

amount of chloride, the corrosion products contained a high content of  $\beta$ -FeOOH. As the corrosion products accumulated, the supply of fresh chlorine did not decrease due to the voids and microcracks in the rust layer.

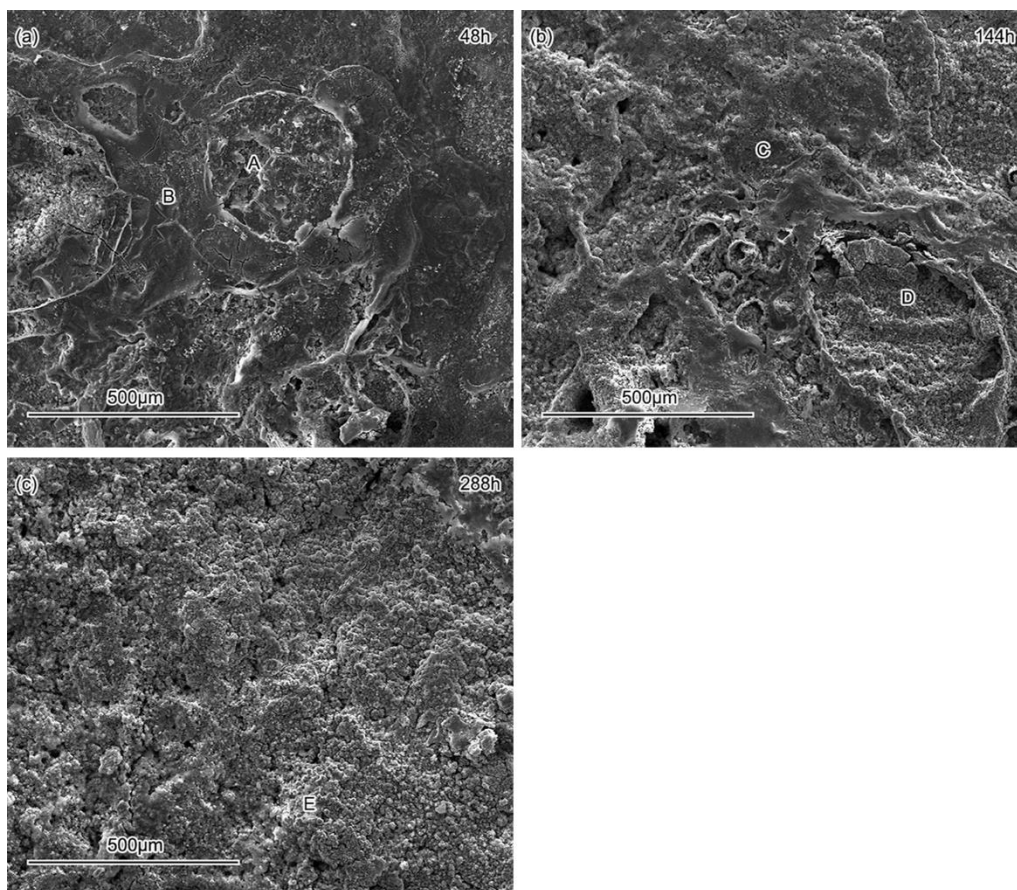


**Figure 4.** The surface morphology of rust layer formed on carbon steel after different corrosion time.

**Table 2.** Elemental contents of the marked sites (wt.%).

site	Fe	O	Cl	S	Na	Mg
A	55.04	43.43	1.53			
B	57.07	40.86	2.07	-	-	
C	51.78	37.98	5.47	0.70	4.06	
D	50.70	27.38	9.17	0.72	12.03	
E	80.02	17.76	2.22	-	-	1.39

The cross-sectional morphologies can better reveal the layer structure of the corrosion products. Figure 5. depicts the cross-sectional morphologies of the rust layers. It can be seen that the rust layer gradually became thicker, and there were many pores and cracks in the rust layer due to a prolonged period of corrosion time. After 288 h, the rust layer appeared complicated. To distinguish the composition of elements in the rust on the steel, the map scanning was performed. The results are shown in Figure 6. A small amount of S and a large amount of chlorine (Cl) were detected in the rust. The Cl distributed in the middle layer and the interface promoted the further corrosion. Sodium (Na) was found to be distributed in the middle layer, which might be caused due to the accumulation of seawater, and calcium (Ca) was detected in the entire rust because seawater contains calcium chloride ( $\text{CaCl}_2$ ) particles. The existence of cations, such as  $\text{Ca}^{2+}$  and  $\text{Mg}^{2+}$ , can promote more anion ( $\text{Cl}^-$  and  $\text{SO}_4^{2-}$ ) adsorption. Consequently, it can be postulated that the corrosion process was affected by both anions and cations in seawater in the “three highs” atmosphere.

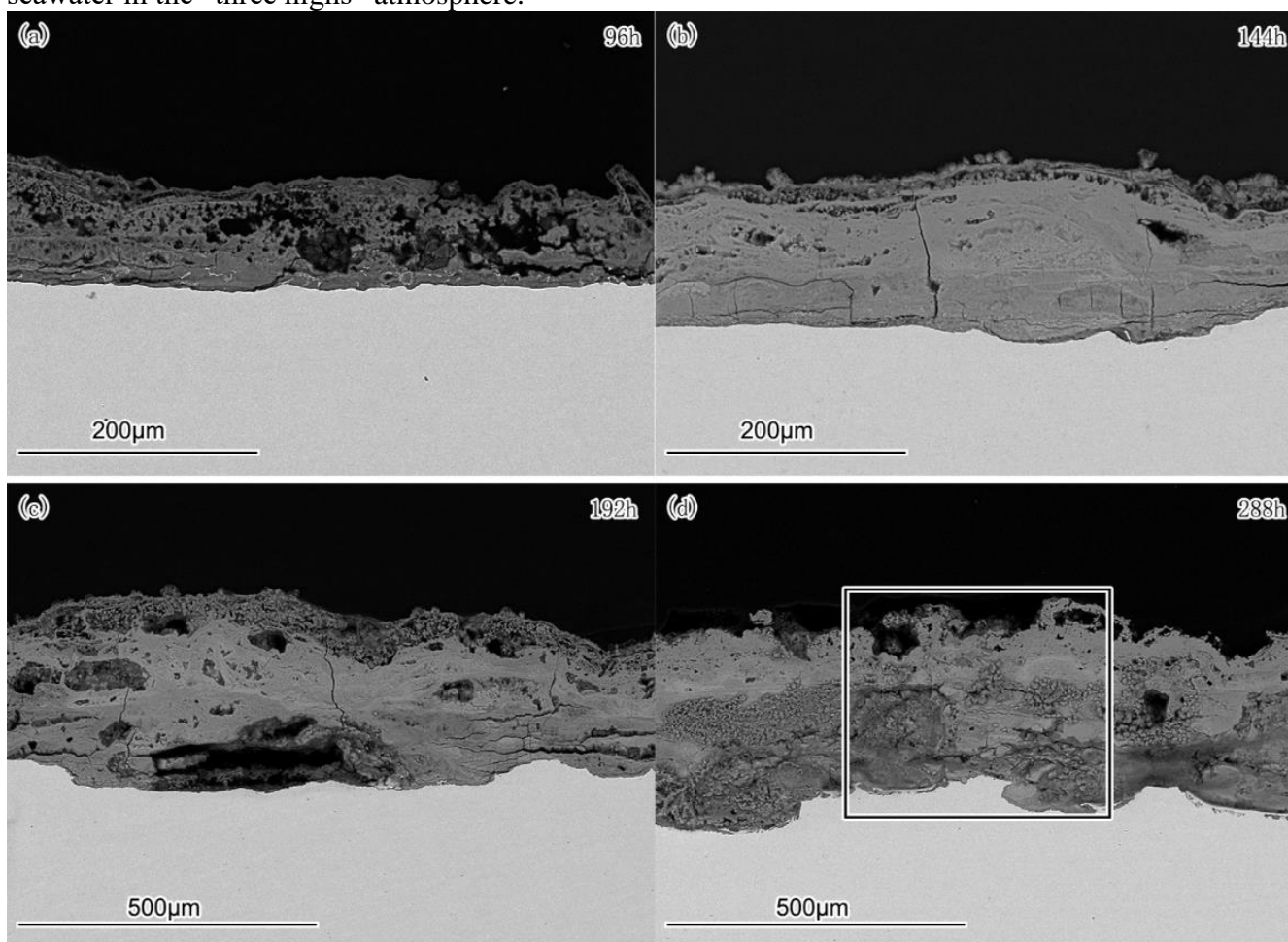


**Figure 5.** The cross-section morphology of rust layer formed on carbon steel after different corrosion time.

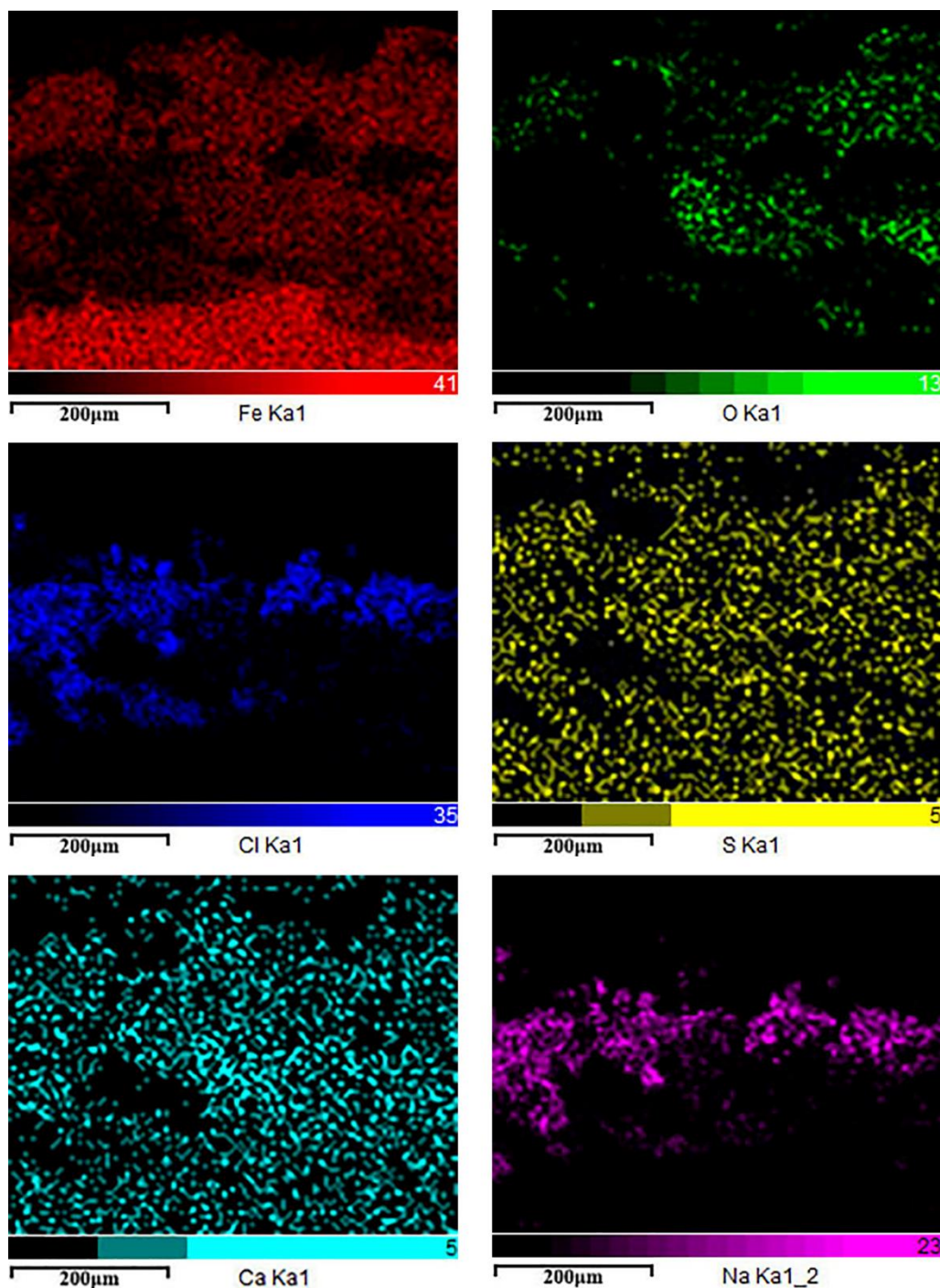


**Figure 6.** The distribution of Fe, O, Cl, S, Ca and Na in the rust formed on the carbon steel surface after 288h. [Map scanning of the portion in Figure 5 (d)]

### 3.3 Electrochemical characteristics of the rust layer

The atmospheric corrosion is essentially an electrochemical reaction taking place under a thin liquid film. Thus, the electrochemical measurement used to evaluate the protectiveness of the rust layer formed on carbon steel appears rational. Consequently, in this study, the potentiodynamic polarization

was adopted as employed in many previous research works [2, 24, 25], and in-situ EIS was also used to monitor the instantaneous corrosion mechanism of carbon steel samples.

Figure 7 depicts the potentiodynamic polarization curves of unruled and rusted steel samples in 0.1 mol/L of  $\text{Na}_2\text{SO}_4$  solution. The cathodic polarization curve of unruled sample was quite different from the rusted ones, implying differences in the reaction process and corrosion mechanism. In addition, the cathodic currents of rusted steels were much larger than the unruled one. This probably was due to the dissolution of ions [12, 15]. With the increasing corrosion time, the cathodic current gradually increased and the anodic current decreased, indicating that the reduction process of corrosion products was the main cathodic reaction, and the anodic process was partially inhibited by the rust layer due to the accumulation of the corrosion products [15]. It is already established that this environment, containing a high amount of chlorine ions, promotes the generation of  $\beta\text{-FeOOH}$  and  $\gamma\text{-FeOOH}$ . Although these products would be reduced during the wetting procedure, they caused the cathodic current density to increase, and then facilitated the corrosion process. This may be a reason that caused an increase in the corrosion rate.

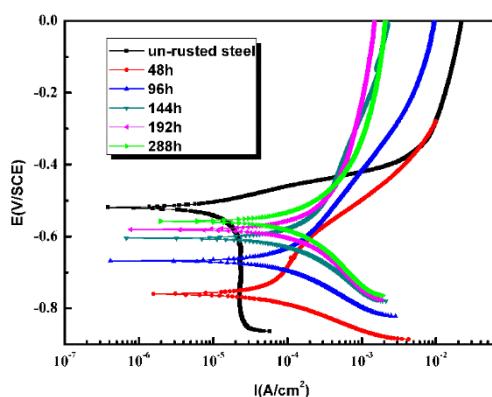


**Figure 7.** Potentiodynamic polarization curves of unruled and rusted steels in 0.1%  $\text{Na}_2\text{SO}_4$  electrolyte as a function of corrosion time.

The properties of the rust layer was further investigated by performing in-situ EIS analysis that can provide more instantaneous corrosion data in a continuous process. Figure 8. shows the Nyquist plots for carbon steel as a function of corrosion time in “three highs” marine atmosphere of the south sea. For the rusted steel samples, the Nyquist diagrams show two depressed semicircles after 48 h and 96 h. The high frequency and the low frequency capacitive loops were related to the rust layer and the charge-transfer process, respectively. With the increase in the corrosion time, more rust accumulated. Consequently, a Warburg impedance appeared after 144 h, indicating the occurrence of a diffusion-controlled corrosion process on the surfaces of samples containing the anodic diffusion process of soluble ferric and the cathodic diffusion of dissolved oxygen [26, 27]. The depressed semicircles were attributed to the dispersion of time constant, which might be caused due to the roughness of surface and/or heterogeneities in metal/electrolyte interface [19, 28]. Accordingly, two equivalent circuits, shown in Figure 9 (a) and 9(b), were used to fit these characteristic impedances. The fitting parameters are given in Table 3. and the fitting lines are shown in Figure 8. as solid lines. The smaller value of the

standard deviation,  $\chi^2$  (in the order of  $10^{-5}$ ), indicated that the equivalent circuits fit coincided well with the test data. In Figure 9,  $R_s$  is the electrolyte resistance,  $Q_r$  and  $R_r$  are the rust layer capacitance and resistance, respectively,  $Q_{dl}$  and  $R_t$  are double layer capacity and the charge transfer resistance, respectively [29, 30], and  $Z_w$  is the barrier diffusion impedance that is associated with the diffusion of corrosive electrolyte on the steel surface through pores in the rust layer that acts as a diffusion barrier [2, 31]. The rust layer resistance  $R_r$  provides information about the hinder ability of the rust layer during the corrosion process. Hence, it is proved to be an important parameter for evaluating the protective properties of the rust layers. The smaller the value of  $R_r$ , the less protective is the rust layer. From Table 3, it can be clearly seen that the values of  $R_r$  fluctuated with time. All the values were quite small, which reflected that the rust layer had no barrier function and it could not effectively prevent the further corrosion reaction. The small value must be attributed to the structure of rust with holes and cracks as shown in Figure 5. The gradual reduction of  $R_t$  for a prolonged period of time might be caused due to the acceleration of the corrosion products reduction reaction. It was in agreement with the results of potentiodynamic polarization. As known that the corrosion rate was usually calculated using the values of polarization resistance ( $R_p$ ) [32]. Compared to  $R_p$ , the charge transfer resistance  $R_t$  can better reflect the corrosion rate because  $R_t$  is only in connection with the faradaic processes of the charge transfer-controlled corrosion. Particularly when the impedance response displays more than one time constant, using  $R_p$  to calculate the corrosion rates will provide incredible results [9, 33]. According to the above analysis,  $R_t$  was taken as an effective parameter to express the corrosion rate of carbon steel. Figure 10. displays the evolution of  $R_t$  values with the increasing corrosion time. Clearly,  $R_t$  decreases significantly at the beginning and becomes stable after 120 h, which is in agreement with the variation of corrosion rates, shown in Figure 2 (b).

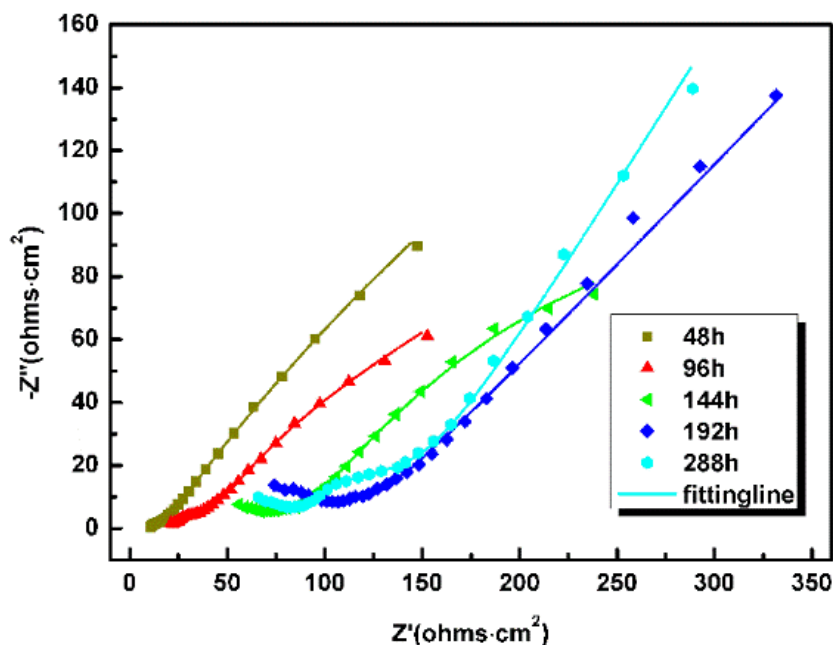
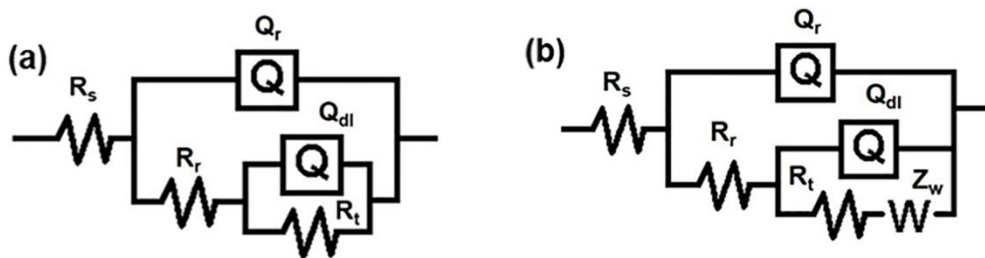


Figure 8. Nyquist diagrams of carbon steel exposed after different corrosion time.



**Figure 9.** Equivalent circuit models used to fit the experimental impedance data for carbon steel (a) 48h and 96h (b) 144h, 192h and 288h

**Table 3.** EIS fitting parameters in equivalent circuits.

Corrosion time/hours	48	96	144	192	288
$R_s$ ( $\Omega \cdot \text{cm}^2$ )	9.934	19.06	46.47	18.64	20.02
$Q_r$ ( $\text{F} \cdot \text{cm}^{-2}$ )	3.07E-03	5.79E-03	1.82E-07	3.50E-05	4.62E-05
$n_r$	0.4294	0.3039	0.9156	0.3949	0.3818
$R_r$ ( $\Omega \cdot \text{cm}^2$ )	9.276	36.18	2.737	86.36	68.18
$Q_{dl}$ ( $\text{F} \cdot \text{cm}^{-2}$ )	1.68E-02	1.32E-02	5.38E-03	5.20E-03	1.90E-03
$n_{dl}$	0.4573	0.4877	0.19	0.3413	0.4952
$R_t$ ( $\Omega \cdot \text{cm}^2$ )	1083	482.8	110.9	79.66	69.14
$Z_w$	-	-	7.80E-03	7.04E-05	1.74E-02
$\sum \chi^2 (\times 10^{-4})$	101	0.573	0.166	0.212	0.625

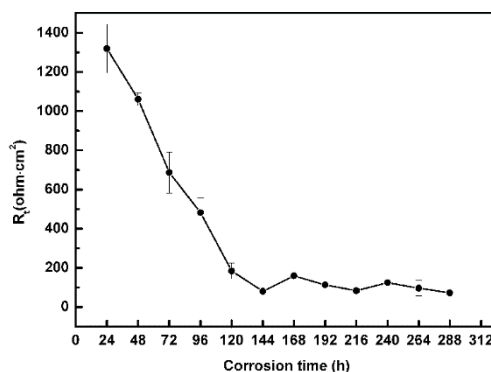


**Figure 10.** Plot of  $R_t$  values of carbon steel as a function of corrosion time.

### 3.4 Composition of the rust layer

The corrosion rate at different exposure periods is related to the composition and/or structure of the rust layer. Figure 11. shows the XRD spectra of the powdered rust on carbon steel samples. The rust

layers during different periods of corrosion time were mainly composed of akaganeite ( $\beta$ -FeOOH), lepidocrocite ( $\gamma$ -FeOOH), a slight amount of goethite ( $\alpha$ -FeOOH), and magnetite ( $\text{Fe}_3\text{O}_4$ ).

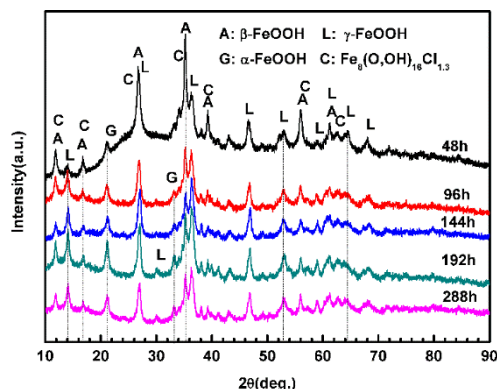


**Figure 11.** X-ray diffraction patterns of the powdered rust formed on the carbon steels

Figure 12. shows the IR spectra of the powdered rust formed on the carbon steel samples to further identify the composition of the rust layers. The results of IR spectra were compared to the reference spectra [10, 14]. The absorption peaks at  $793\text{ cm}^{-1}$  corresponded to the O-H bending in  $\alpha$ -FeOOH [14, 34, 35]. A wide absorption band around  $1615\text{ cm}^{-1}$  was caused due to the vibration of Fe-O bonds in  $\beta$ -FeOOH. The peaks at  $1020\text{ cm}^{-1}$  and  $1110\text{ cm}^{-1}$  were due to the O-H bending in  $\gamma$ -FeOOH and  $\delta$ -FeOOH, respectively. Hence, the IR spectra indicated that the corrosion products were mainly composed of  $\beta$ -,  $\gamma$ -, Ferrihydrite ( $\delta$ -FeOOH) and a slight amount of  $\alpha$ -. The relative amount of  $\delta$ - and  $\gamma$ - in the rust increased for a prolonged period of time, whereas the amount of  $\beta$ - was almost stable. As known, FeOOH has four types of isomers:  $\beta$ -,  $\gamma$ -,  $\delta$ -, and  $\alpha$ - [34], where  $\alpha$ - is an electrochemically stable phase, whereas  $\beta$ -,  $\gamma$ -, and  $\delta$ - are all electrochemically active phase and can be easily reduced to relatively stable magnetite [36]. The reduction order of various rust components decreased as follows [37, 38]:  $\delta > \beta > \text{Fe}_3\text{O}_4 > \gamma > \alpha$ . Indeed,  $\beta$ - is not a single phase parameter that contains a certain amount of  $\text{Cl}^-$  [34], which can be clearly seen from the XRD spectrum shown in Figure 11.

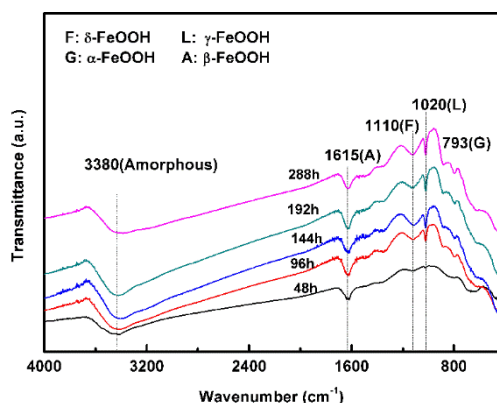
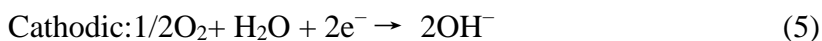


**Figure 12.** IR spectra of the powdered rust formed on the carbon steels.

The results of IRS and XRD together indicated that a large amount of  $\beta$ -FeOOH existed in the rust layer, which is closely related to the abundant  $\text{Cl}^-$  in the “three highs” atmosphere of the south sea. However, the foreign elements Ca and Mg were not detected in the corrosion products, which might be in the form of free ions in the rust layer. According to the protective ability index (PAI) in a previous study [36], the value of the mass ratio “ $\alpha/\gamma^*$ ” was very small in this study, around 0.2, indicating that the rust layer had no protective effect with the increasing time.

Based on the above analysis, in the initial stage, the primary electrochemical reactions could be as follows [39, 40]:



At the beginning of the corrosion process, the ferrous ions and hydroxyl moved to the cathodic area and anodic area, respectively.  $\text{Fe}(\text{OH})_2$  was generated on the active anode area, then  $\text{Fe}(\text{OH})_2$  rapidly oxidized into Fe(II) and Fe(III) oxides. These preliminary corrosion products were subsequently transformed into  $\alpha$ -FeOOH,  $\beta$ -FeOOH,  $\gamma$ -FeOOH,  $\delta$ -FeOOH, and  $\text{Fe}_3\text{O}_4$ . Among these corrosion products, the formation of  $\beta$ -FeOOH was associated with the abundant amount of  $\text{Cl}^-$ , whereas  $\gamma$ -FeOOH was formed partially due to the re-crystallization of  $\beta$ -FeOOH or due to the crystallization of amorphous oxides [28]. The formation of  $\gamma$ -FeOOH involved the following process: during the wetting procedure, the electrons produced by the anodic dissolution of iron were consumed by a reduction reaction. However, as the corrosion process progressed, the dissolved oxygen as an oxidizer could not be reduced on the rust layer because the rust layer was not conductive. The cathodic reaction changed into the reduction of  $\gamma$ -FeOOH as follows:



$\gamma\text{-Fe} \cdot \text{OH} \cdot \text{OH}$ , formed as an intermediate product on the surface of  $\gamma$ -FeOOH, could transform into both  $\text{Fe}_3\text{O}_4$  and  $\alpha$ -FeOOH [41, 42]. During the drying stage, the  $\gamma$ -FeOOH gradually regenerated from  $\gamma\text{-Fe} \cdot \text{OH} \cdot \text{OH}$ . Hence, a series of process was repeated several times when the wetting of rust was repeated. As a result, a recurrent generation-transformation-regeneration cycle of  $\gamma$ -FeOOH was formed. Combined with the above roughness analysis, the generation-transformation-regeneration of  $\gamma$ -FeOOH might be the main reason for the roughness change of the rust layer for a prolonged period of corrosion time. The occurrence of cracking in the rust layer promoted the anion and cation permeate to the substrate, causing the further dissolving of steel and  $\text{Fe}(\text{OH})_2$ , and increasing the corrosion rate.

#### 4. CONCLUSION

The influence of seawater on the carbon steel initial corrosion behavior, exposed to the “three highs” marine atmosphere of the south sea, was investigated. Conclusions can be drawn as follows:

1. The experimental results indicate that with corrosion time prolonged, the kinetics of corrosion process follow empirical equation  $D=At^n$ .
2. The rust layer has no protective effect for the reason of the change of roughness on rust surface and the existence of voids and microcracks in rust layer.
3. The main composition of the rust layer were  $\beta$ -FeOOH,  $\gamma$ -FeOOH,  $\delta$ -FeOOH, slightly

$\alpha$ -FeOOH, and Fe<sub>3</sub>O<sub>4</sub> for all corrosion periods. As the corrosion time increased, the content of  $\delta$ -FeOOH and  $\gamma$ -FeOOH in the rust increased, whereas the content of  $\beta$ -FeOOH was almost stable. Although, the value of the mass ratio " $\alpha/\gamma^*$ " was very small.

4. The decrease of the charge transfer resistance ( $R_t$ ) measured by in-situ EIS instantaneously indicated that the corrosion rate was increased gradually with increasing time.

#### ACKNOWLEDGEMENTS

This work was financially supported by the Strategic Priority Research Program of the Chinese Academy of Science (No.XDA13000000), Guangzhou Industry-university-research Collaborative Innovation Alliance Special Project (No.201604046014) and National Natural Science Foundation of China (No. 51671197).

#### References

1. S. Syed, *Corrosion*, 61 (2010) 238.
2. Q.X. Li, Z.Y. Wang, W. Han, E.H. Han, *Corros. Sci.*, 50 (2008) 365.
3. Y. Ma, Y. Li, F. Wang, *Mater.Chem. Phys.*, 112 (2008) 844.
4. B.Y.R. Surnam, C.V. Oleti, *Corros. Eng., Sci. Technol.*, 47 (2013) 446.
5. T.T.N. Lan, N.T.P. Thoa, R. Nishimura, Y. Tsujino, M. Yokoi, Y. Maeda, *Corros. Sci.*, 48 (2006) 179.
6. S.X. Li, L.H. Hihara, *Corros. Eng., Sci. Technol.*, 45 (2013) 49.
7. W. Chen, L. Hao, J. Dong, W. Ke, *Corros. Sci.*, 83 (2014) 155.
8. C. Arroyave, F.A. Lopez, M. Morcillo, *Corros. Sci.*, 37 (1995) 1751.
9. C. Pan, W. Ly, Z. Wang, W. Su, C. Wang, S. Liu, *J. Mater. Sci. Technol.*, 33 (2017) 587.
10. D. Mizuno, S. Suzuki, S. Fujita, N. Hara, *Corros. Sci.*, 83 (2014) 217.
11. F. Mansfeld, *J. Electrochem. Soc.*, 135 (1988) 1354.
12. F. Mansfeld, J.V. Kenkel, *Corros. Sci.*, 16 (1976) 111.
13. A. Tahara, T. Kodama, *Corros. Sci.*, 42 (2000) 655.
14. A.K. Neufeld, I.S. Cole, A.M. Bond, S.A. Furman, *Corros. Sci.*, 44 (2002) 555.
15. C. Li, Y. Ma, Y. Li, F. Wang, *Corros. Sci.*, 52 (2010) 3677.
16. C. Thee, L. Hao, J. Dong, X. Mu, X. Wei, X. Li, W. Ke, *Corros. Sci.*, 78 (2014) 130.
17. X. Chen, J. Dong, E. Han, W. Ke, *Mater. Lett.*, 61 (2007) 4050.
18. X. Zhang, S. Yang, W. Zhang, H. Guo, X. He, *Corros. Sci.*, 82 (2014) 165.
19. Y. Ma, Y. Li, F. Wang, *Mater. Chem.Phys.*, 112 (2008) 844.
20. M. Natesan, G. Venkatachari, N. Palaniswamy, *Corros. Sci.*, 48 (2006) 3584.
21. S. Syed, *Corros Eng., Sci. Technol.*, 45 (2013) 282
22. L. Hao, S. Zhang, J. Dong, W. Ke, *Corros. Sci.*, 54 (2012) 244.
23. Y.Y. Chen, H.J. Tzeng, L.I. Wei, H.C. Shih, *Mater. Sci., Eng. A*, 398 (2005) 47.
24. J. Wang, Z.Y. Wang, W. Ke, *Mater. Chem. Phys.*, 124 (2010) 952.
25. A.P. Yadav, A. Nishikata, T. Tsuru, *Corros. Sci.*, 46 (2004) 361.
26. C. Pan, W. Lv, Z. Wang, W. Su, C. Wang, S. Liu, *J. Mater. Sci. Technol.*, 33 (2017) 587.
27. G. Žerjav, I. Milošev, *Corros. Sci.*, 98 (2015) 180.
28. T. Misawa, K. Hashimoto, S. Shimodaira, *Corros. Sci.*, 14 (1974) 131.
29. Y. Liu, Z. Wang, W. Ke, *Corros. Sci.*, 80 (2014) 169.
30. Z. Cui, X. Li, K. Xiao, C. Dong, *Corros. Sci.*, 76 (2013) 243.
31. L. Hao, S. Zhang, J. Dong, W. Ke, *Corros. Sci.*, 59 (2012) 270.
32. K.-W. Chung, K.-B. Kim, *Corros. Sci.*, 42 (2000) 517.
33. Y. Cheng, Z. Zhang, F. Cao, J. Li, J. Zhang, J. Wang, C. Cao, *Corros. Sci.*, 46 (2004) 1649.

34. C.B. Breslin, D.D. Macdonald, J. Sikora, E. Sikora, *Electrochim. Acta*, 42 (1997) 127.
35. C.B. Breslin, D.D. Macdonald, E. Sikora, J. Sikora, *Electrochim. Acta*, 42 (1997) 137.
36. T. Kamimura, S. Hara, H. Miyuki, M. Yamashita, H. Uchida, *Corros. Sci.*, 48 (2006) 2799.
37. H. Antony, S. Perrin, P. Dillmann, L. Legrand, A. Chaussé, *Electrochim. Acta*, 52 (2007) 7754.
38. C. Pan, W. Han, Z. Wang, C. Wang, G. Yu, *J. Mater. Eng. Perform.*, 25 (2016) 5382.
39. X. Zhang, K. Xiao, C. Dong, J. Wu, X. Li, Y. Huang, *Eng. Fail. Anal.*, 18 (2011) 1981.
40. Y.Y. Chen, H.J. Tzeng, L.I. Wei, L.H. Wang, J.C. Oung, H.C. Shih, *Corros. Sci.*, 47 (2005) 1001.
41. I.M. Allam, J.S. Arlow, H. Saricimen, *Corros. Sci.*, 32 (1991) 417
42. M. Stratmann, K. Bohnenkamp, H.J. Engell, *Corros. Sci.*, 23 (1983) 969.

© 2019 The Authors. Published by ESG ([www.electrochemsci.org](http://www.electrochemsci.org)). This article is an open access article distributed under the terms and conditions of the Creative Commons Attribution license (<http://creativecommons.org/licenses/by/4.0/>).